Colloids and Surfaces A: Physicochem. Eng. Aspects 522 (2017) 173–182

Contents lists available at ScienceDirect

Colloids and Surfaces A: Physicochemical and Engineering Aspects

journal homepage: www.elsevier.com/locate/colsurfa

Spray drying assisted assembly of ZnO nanocrystals using cellulose as sacrificial template and studies on their photoluminescent and photocatalytic properties

Yanan Yuan[a,b], Aiping Fu[b], Yiqian Wang[c], Peizhi Guo[a,b], Guanglei Wu[a,b], Hongliang Li[a,b,*], Xiu Song Zhao[a,b,d]

[a] Institute of Materials for Energy and Environment, Qingdao University, 266071 Qingdao, China
[b] Laboratory of New Fiber Materials and Modern Textile, Growing Basis for State Key Laboratory, College of Materials Science and Engineering, Qingdao University, 266071 Qingdao, China
[c] College of Physics, Qingdao University, No. 308 Ningxia Road, 266071 Qingdao, China
[d] School of Chemical Engineering, The University of Queensland, 4074 Brisbane, QLD, Australia

HIGHLIGHTS

- Spray drying technique was utilized for the preparation of ZnO nanocrystal assemblies using zincoxen cellulose solution as raw materials.
- Zincoxen plays both the role as solvent for cellulose and precursor for the ZnO nanocrystals.
- Cellulose acts as assembly agent during the spray drying step and sacrificial templates in the calcinations process.
- The content of cellulose and the calcination temperature influence the properties of the resulted ZnO nanocrystal assemblies.
- The assemblies of ZnO nanocrystals exhibit high photocatalytic activity for methyl orange degradation in aqueous solution.

GRAPHICAL ABSTRACT

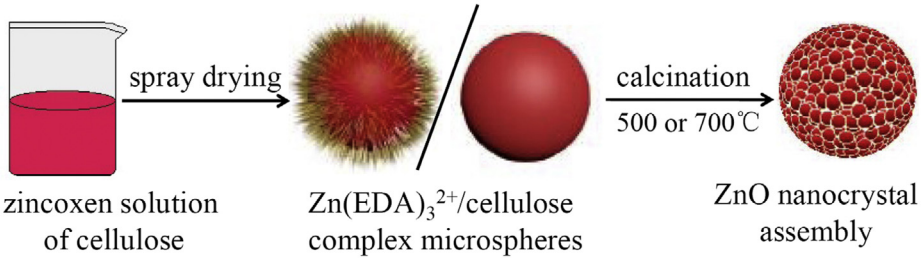

Zincoxen cellulose solution was used as raw materials for the preparation of zincoxen/cellulose complex microspheres via a spray drying process. The obtained zincoxen/cellulose microspheres were turned into assemblies of ZnO nanocrystals upon calcinations at 500 or 700 °C. The assemblies of ZnO nanocrystals exhibit high photocatalytic activity for methyl orange degradation under ultraviolet light irradiation in aqueous solution and also satisfied reusability and stability of morphology and composition.

ARTICLE INFO

Article history:
Received 21 August 2016
Received in revised form 7 February 2017
Accepted 23 February 2017
Available online 27 February 2017

Keywords:
Spray drying
ZnO nanocrystal assembly
Zincoxen cellulose solution
Sacrificial template
Photoluminescence
Photocatalyst

* Corresponding author. Tel.: +86 53285950767.
E-mail address: lhl@qdu.edu.cn (H. Li).

http://dx.doi.org/10.1016/j.colsurfa.2017.02.068

ABSTRACT

The conventional zincoxen cellulose solution, which was obtained by dissolving cellulose with the zincoxen solvent (tri(ethylenediamine) zinc hydroxide solution, $Zn(EDA)_3^{2+}$), has been used as raw materials for the preparation of zincoxen/cellulose complex microspheres via a spray drying technique. The obtained zincoxen/cellulose microspheres are turned into assemblies (or clusters) of ZnO nanocrystals by calcining the complex microspheres at 500 or 700 °C. For the preparation, zincoxen plays both the role as solvent for cellulose and precursor for the ZnO nanocrystals. While, the cellulose acts as assembly agent during the spray drying step and sacrificial templates in the calcinations process. The content of cellulose in the zincoxen cellulose aqueous solution and the calcination temperature show significant impacts on the morphology, porosity, optical properties and photocatalytic activity of the resulted ZnO nanocrystal assemblies. The structures, morphology and porosity have been investigated based on XRD, SEM, TEM and N_2 adsorption-desorption technique.

The lattice parameters have been fitted by the Rietveld refinement and the strains in the crystals have been studied. Under ultraviolet light irradiation, all the assemblies of ZnO nanocrystals exhibit high photocatalytic activity for methyl orange degradation in aqueous solution and also satisfied reusability and stability of morphology and composition.

1. Introduction

Zinc oxide (ZnO) is a wide band gap semiconductor (Eg = 3.37 eV) with a large exciton binding energy of 60 meV, making ZnO a good candidate for photocatalytic applications [1,2]. ZnO nanostructure can be synthesized in various morphologies such as nanotubes [3], nanorods [4], nanobelts [5], nanowalls [6], nanowires [7], nanoflakes [8] and nanoflowers [9]. It has been reported that the photocatalytic activity of ZnO nanostructures are heavily dependent on their crystal structures and the surface morphologies [10,11]. Up to date, several techniques have been documented for the synthesis of ZnO nanostructures with different morphologies such as chemical vapor deposition (CVD) [12], vapor–liquid–solid (VLS) growth [13], sol-gel method [14] and hydrothermal solution method [15]. However, most of the reported methods require severe conditions or catalysts for ZnO growth, and it is also difficult to obtain ZnO nanocrystals in large scale. As a mass-producible technique and industrial preparation method, spray drying is rare referred to in the preparation of ZnO nanocrystals, especially an assembly of them [16].

Cellulose has attracted intense attention due to its biocompatibility, biodegradability and renewability, and it has been exploited as a promising raw material in chemical, biological, and energy industries [17]. However, natural cellulose possesses strong inter- and intra-molecular hydrogen bonding caused by the hydroxyl groups. Therefore, it neither melts at high temperature nor dissolves in common aqueous solvents, limiting its application with morphology requirement. Traditional solvent systems such as cuprammonia, zincoxen and FeTNa (ferric tartaric acid complex) were utilized for the dissolving of cellulose [18]. However, the application of the resultant cellulose solutions focus mainly on structure or molecular weight studies on cellulose and/or used as solvent for fabrication of fiber in textile industry.

In this paper, we report on a flexible approach to the assembly of ZnO nanocrystals using zincoxen cellulose solution as precursors by the large-scale producible technique namely spray drying and combining a successively calcinations process. Assemblies (or clusters) consisting of ZnO nanocrystals with different sizes were derived after the calcinations at 500 and 700 °C, respectively. For the total preparation, the zincoxen species played two different roles, i.e., as a solving agent in the preparation of zincoxen cellulose aqueous solution and as a precursor for the ZnO nanocrystals. The influences of calcination temperature and content of cellulose on the crystal structures, surface morphology, specific surface area and photoluminescent properties of the resultant assemblies have been investigated. The lattice parameters of the resulted ZnO nanocrystals have been fitted by the Rietveld refinement and the strains in them have been studied. The assemblies of ZnO nanocrystal exhibit great potential for photocatalytic application, and the effect factors on the photocatalytic ability for the degradation of methyl orange have been explored. The ZnO nanocrystal assemblies turn out to be a structurally ideal photocatalyst that can provide more active sites and favorable transport pathways of electrons and holes, posses also the advantages of recyclability, and structural and compositional stability [19–22].

2. Experimental

2.1. Materials

Cellulose with a viscosity-average molecular weight of 8.5×10^4 was obtained from Hailong Chemical Fiber Co., Ltd. Sodium hydroxide, zinc chloride, anhydrous ethylenediamine and methyl orange (MO) were analytical grade and used as received without further purification. Distilled water was used in all the experiments.

2.2. Preparation of zincoxen solution of cellulose

Ethylenediamine (EDA) was diluted to 30% and left in refrigerator as a standby. NaOH aqueous solution was added into zinc chloride aqueous solution dropwise until the Zn(II) was precipitated completely, forming fresh-prepared zinc hydroxide precipitation. The white sediment was separated by centrifugation and washed five times with distilled water. The fresh-prepared precipitate was then dissolved partly by the 30% aqueous ethylenediamine under stirring, resulting in zincoxen aqueous solution [23]. The zincoxen aqueous solution was purified with high speed centrifugation and was then used as solvent for the dissolution of cellulose. First, cellulose was dispersed in precooled zincoxen aqueous solution to −10 °C overnight and then thawed at room temperature, obtaining a homogeneous zincoxen cellulose solution ($Zn(EDA)_3^{2+}$/cellulose).

2.3. Preparation of the assemblies of ZnO nanocrystals

First, the $Zn(EDA)_3^{2+}$/cellulose complex microspheres were prepared by a spray drying process using the zincoxen aqueous solution of cellulose as starting materials through a laboratory-scale SP-1500 spray dryer (Shanghai SunYi Tech Co., Ltd.). The imported zincoxen cellulose aqueous solution was pulverized by the shear forces of the pressurized air with a pressure in the range of 200–400 kPa, spraying out tiny droplets of zincoxen cellulose aqueous solution through the orifice of the nozzle on the spray dryer. The moisture in these droplets are quickly evaporated upon direct contacting with the 130 °C hot air flow which passed through the chamber, resulting in drying-out and stable $Zn(EDA)_3^{2+}$/cellulose complex in powder form. The powders were collected by an integrated cyclone separator. The $Zn(EDA)_3^{2+}$/cellulose complex microspheres derived from zincoxen cellulose aqueous solution with different cellulose content were labeled as x%-Z/C (x = 1.25, 2.5, 3.75 and 5.0), where the numbers in the brackets refer to the grams of cellulose dissolved in 100 g of zincoxen cellulose solution. Assemblies of ZnO nanocrystals were then facilely prepared by calcining the $Zn(EDA)_3^{2+}$/cellulose complex microspheres in a programed tubular furnace at 500 or 700 °C, respectively, in air atmosphere for 3 h. The resulted samples were designated as x%-ZnO-500 and x%-ZnO-700 (x = 1.25, 2.5, 3.75 and 5.0), respectively, where 500 and 700 represent the calcination temperature, whereas the numbers in the brackets corresponding to the contents of cellulose as mentioned above. An illustration of the formation process of the ZnO nanocrystal assembly is depicted in Scheme 1.

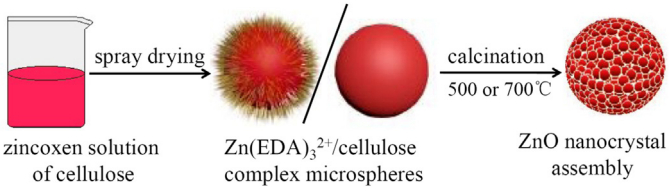

Scheme 1. Illustration of the formation process of the ZnO nanocrystal assembly.

2.4. Photocatalytic degradation of methyl orange

The photocatalytic activity of the ZnO nanocrystal assemblies was investigated by monitoring the degradation of MO under the illumination of UV light using the ZnO assembly as photocatalyst. A commercial UV lamp with output power of 125 W and wavelength of 365 nm was utilized for the irradiation. For the degradation experiment, 0.1 g of catalyst was dispersed in 100 mL of MO aqueous solution with a concentration of 10 mg/L. Then the suspension was magnetically stirred in dark for 1 h to ensure the establishment of an adsorption–desorption equilibrium. Subsequently, the suspension was subjected to UV light irradiation. At given time intervals, 4 mL aliquots were collected and then centrifuged to remove the photocatalyst particles. The concentration of methyl orange was determined by checking the absorbance using an UV–vis spectrophotometer. As control experiments, similar operations were also performed without the photocatalyst or in the absence of UV irradiation. To test the recyclability of the catalyst, photodegradation of MO in five consecutive cycles was performed employing a definite amount of ZnO catalyst. In the successive cycles, the catalyst was washed with distilled water several times and used for the next cycling. After the fifth cycle, the catalyst was collected by centrifugation and air drying. The stability of the composition and structure of the ZnO assemblies after five cycles of the photocatalytic reaction has been studied by monitoring their XRD patterns and SEM images.

2.5. Characterizations

The crystal structures and the surface morphologies of the samples were analyzed using a JEOL JSM-7800F scanning electron microscopy (SEM) instrument and a JEOL JEM-2100 transmission electron microscopy (TEM) instrument. The specific surface areas were estimated using the Brunauer–Emmett–Teller (BET) method with an Autosorb-iQ-MP/XR surface area and pore analyzer (Quantachrome Instruments). The phase purity of synthesized powders were studied by X-Ray Diffraction patterns (XRD) using a Rigaku Ultima IV X-ray diffractometer equipped with graphite monochromatized Cu K_α radiation ($\lambda = 0.15418$ nm). UV–vis spectra were measured through a TU-1901 UV–visible spectrophotometer. The photoluminescence (PL) behaviors were investigated by a fluorescence spectrometer (F-4600) with an excitation wavelength of 325 nm.

3. Results and discussion

3.1. XRD measurements

Fig. 1 shows the powder XRD patterns of the x%-ZnO-500 series samples. They show patterns with the same diffraction positions even though the peak intensity is slightly different. Six characteristic peaks were observed at 2θ values of 31.8°, 34.4°, 36.3°, 47.54°, 56.6° and 68.0°, which respectively correspond to the (100), (002), (101), (102), (110), (103) and (112) crystalline planes of a hexagonal wurtzite ZnO phase (PDF No.36-1451). Moreover, no redundant diffraction peak can be observed, which illustrates that the obtained

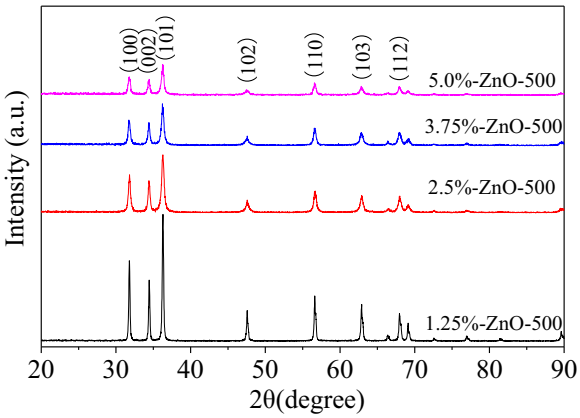

Fig. 1. XRD patterns of the x%-ZnO-500 series samples.

samples are of single phase. Similar XRD patterns were obtained for the x%-ZnO-700 series samples (see Fig. S1).

3.2. SEM and TEM studies

SEM and TEM images of the spraying dried $Zn(EDA)_3^{2+}$/cellulose complex are depicted in Fig. 2. From the images, one can see that all these samples show wrinkled spherical morphology. By comparing images A, B, C and D, it can be seen that zincoxen nanorods distributed in the surface of the complex, while with the increase of the mass content of cellulose in the zincoxen cellulose solution from 1.25 to 5.0%, the superficial zincoxen nanorods decrease and disappear eventually (see image D). The results may be due to the zincoxen is excessive for cellulose dissolution at the low cellulose content. TEM measurements have been carried out to further elucidate the structure of $Zn(EDA)_3^{2+}$/cellulose complex. Fig. 2E presents the TEM images of 1.25%-Z/C sample, and it reveals that redundant zincoxen nanorods diffuse from the inner of the cellulose matrixes to the surface, and some of them are totally or partially encapsulated by cellulose. Fig. 2F and G depicts the TEM images of 2.5%-Z/C and 3.75%-Z/C samples, respectively. It can be seen that zincoxen nanorods decrease with the increase of mass content of cellulose and these results are consistent with the SEM measurements. It has been shown in Fig. 2H, when the content of cellulose reaches to 5 wt% no zincoxen nanorod can be observed on the surface and/or in the internals of the complex spheres. The disappearance of zincoxen rods with the increase of cellulose content can be explained as due to the completely coordinating between zincoxen and cellulose.

Fig. 3 presents the SEM images of both the x%-ZnO-500 and the x%-ZnO-700 series samples, which derived from the corresponding $Zn(EDA)_3^{2+}$/cellulose complex microspheres as are presented in Fig. 2 by calcination under air for 3 h at different temperatures. It can be seen from images of Fig. 3A–D, individual ZnO crystals with size of about several tens nanometers assembled into cluster structures, and the micro-frameworks of the resultant x%-ZnO-500 are similar to its precursor microspheres. Definitely, for x%-ZnO-700 series samples, they also show assembly of ZnO nanocrystals. However, the size of individual ZnO nanocrystal increases to about 100 nm and turn to inhomogeneous, and some crystals with polygon structure can be found among them as shown in Fig. 3E–H. On the basis of SEM and TEM measurements, one can deduce that cellulose act as template during the formation of the clusters and it also affect the crystal morphology of the resultant ZnO crystals. The crystal size decreases and turns to more uniform with the increase of cellulose content in the precursors. The sizes of x%-ZnO-700 series samples made from the same cellulose content are larger than x%-ZnO-500 series ones. The differences between them can be ascribed to the

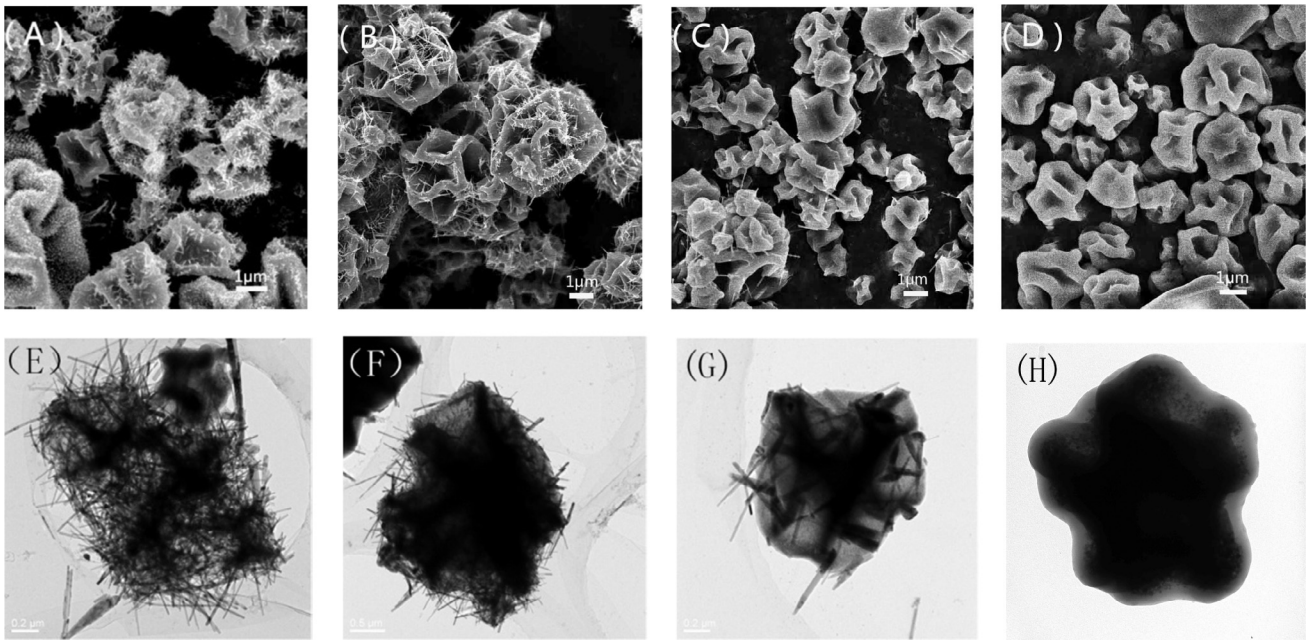

Fig. 2. SEM images of (A) 1.25%-Z/C, (B) 2.5%-Z/C, (C) 3.75%-Z/C, (D) 5.0%-Z/C, and TEM image of (E) 1.25%-Z/C, (F) 2.5%-Z/C, (G) 3.75%-Z/C, and (H) 5.0%-Z/C.

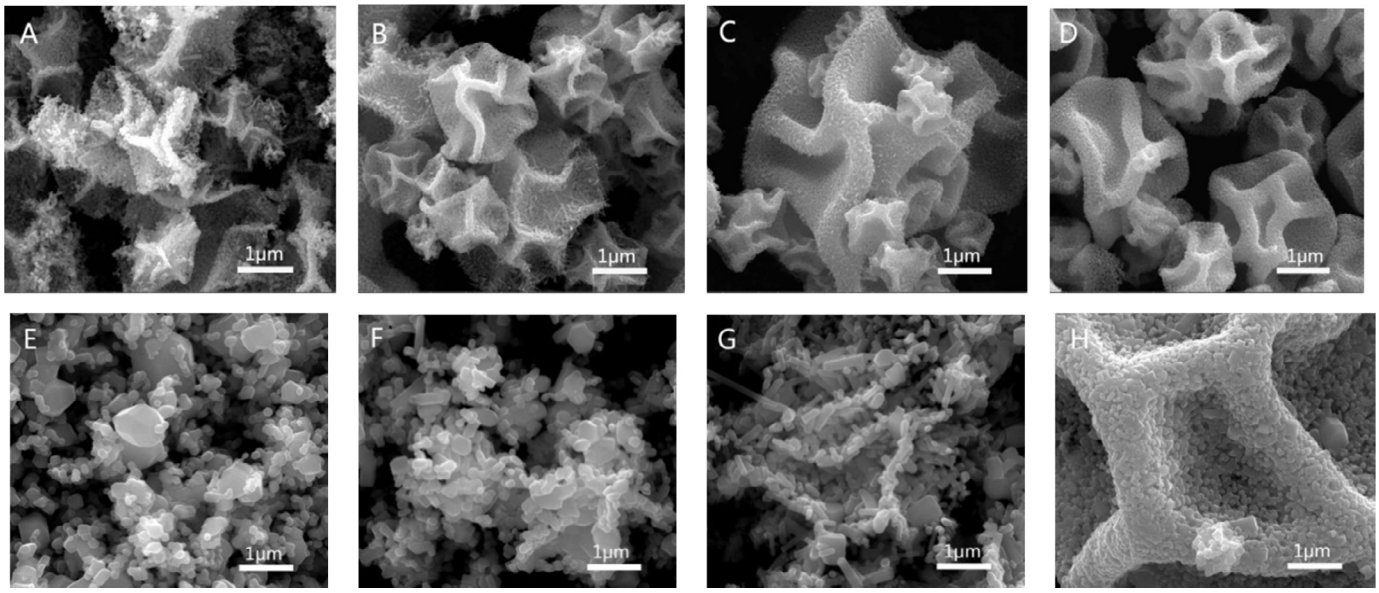

Fig. 3. SEM images of (A) 1.25%-ZnO-500, (B) 2.5%-ZnO-500, (C) 3.75%-ZnO-500, (D) 5.0%-ZnO-500, (E) 1.25%-ZnO-700, (F) 2.5%-ZnO-700, (G) 3.75%-ZnO-700, and (H) 5.0%-ZnO-700.

sintering effect, which induces the growth of the individual crystal at a high temperature.

Fig. 4 depicts the high-resolution TEM image and the selected area electron diffraction (SAED) pattern of an individual ZnO nanocrystal. As can be seen from Fig. 4A, the lattice spacing of 0.28 nm can be calculated, which corresponds to the standard spacing of (100) planes in hexagonal ZnO crystal. The SAED pattern (in Fig. 4B) shows distinct rings consisting of bright spots, and they can be designated to the (100), (101), (102), (110) and (103) planes, confirming further the hexagonal wurtzite structure of ZnO nanocrystal. The result is consistent well with the XRD measurements.

3.3. Rietveld refinement and strain analysis

In order to determine further the phase purity of the samples as well as the lattice parameters, the Rietveld refinement was carried out using the GSAS software based on the XRD data. The phase Rietveld fit of ZnO was performed on the hexagonal wurtzite crystal structure with space group of $P6_{3mc}$ (186) [24]. The initial refinement was done by the scale factor, the lattice parameters, the zero-point shift and background parameters. After achieving a good match of the peak positions, the peak profile parameters including the peak asymmetry were refined. Fig. 5 shows the Rietveld refinement patterns using the X-ray powder diffraction data of 1.25%-ZnO-500 sample as an example. It shows good agreement

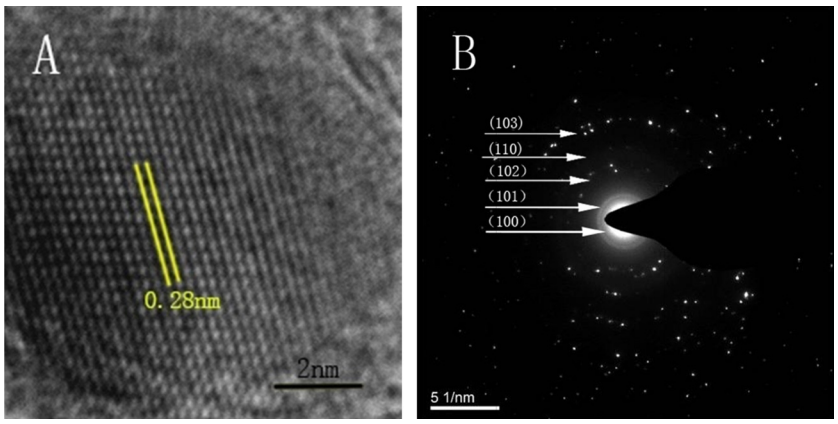

Fig. 4. (A) high-resolution TEM image and (B) selected area electron diffraction pattern of ZnO nanocrystal.

Table 1
Reliability indices, lattice parameters, bond angles and cell volume of 1.25%-ZnO-500 sample.

Rwp	Rp	Lattice parameters/Å		α	β	γ	Cell volume
		a = b	c				
0.1052	0.137	3.24883 (4)	5.20479 (10)	90	90	120	47.5761 (12)

between observed XRD patterns and theoretical fit results, indicating the success of the Rietveld refinement process [25]. It is verified further by small differences near to zero in the intensity scale as illustrated by a line (obs-calc). Values obtained through Rietveld refinement e.g. the reliability indices of the refinement (Rwp, Rp), lattice parameters, bond angles and cell volume are summarized in Table 1. The low values of the reliability indices of Rwp and Rp suggest that the pattern fitting is accurate [26]. From Table 1 it can be seen the calculated lattice crystal parameters of 1.25%-ZnO-500 sample are in good agreement with the observed one, indicating the phase purity of the resulted sample is relatively high.

Strain or stress can be involved in crystals due to the stacking of the crystal and the presence of defects, such as grain boundaries, dislocations, voids, impurities and so on, especially in those as blocks to form a clusters or assemblies [27]. Stresses have been evaluated by a number of techniques, X-ray diffraction is one of the methods used by many authors to assess the stress. The stress values in these samples of our work calculated use the $\sin^2\psi$ method with the JADE software are presented in Fig. S2. It can be seen that the stress values of x%-ZnO-500 series samples are negative, and

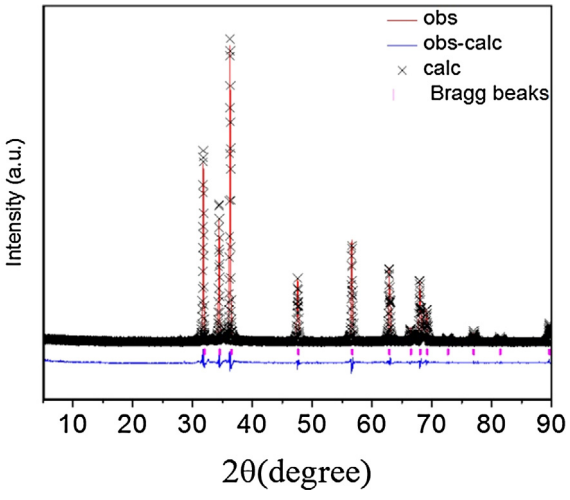

Fig. 5. Rietveld refinement plots of 1.25%-ZnO-500 sample.

such a negative sign indicates a compressive stress. Meanwhile, the compressive stress value increases with the increasing of cellulose content in the precursors. The stress values of x%-ZnO-700 series samples are positive, it is a tensile stress. In terms of the grain boundary relaxation model, it was proposed that the tensile stress is related to voided microstructure at the grain boundary [28]. The different strains in the two series of x%-ZnO samples can be explained as due to the sintering effect at a high temperature.

3.4. Nitrogen adsorption-desorption measurements

N_2 adsorption–desorption measurements were employed to investigate the specific surface area and pore size distributions of the x%-ZnO-500 and x%-ZnO-700 series samples. The isotherms and corresponding pore size distribution curves are shown in Fig. 6. As can be seen, the isotherms of these x%-ZnO-500 (x = 1.25, 2.5 and 3.75) series samples show obvious hysteresis loops and capillary condensation steps (Fig. 6a–c), suggesting the existence of porous structure in them [29]. The corresponding pore size distribution curves (inset) demonstrated that BJH pore size distributions of x%-ZnO-500 series samples locate at around 40 nm. The large sized pore inside the assemblies can be induced by the spacing among the ZnO nanocrystals. For 5.0%-ZnO-500 sample, it shows relatively lower BET surface area, pore volume and average pore width, which is calculated to be only 4.5 $m^2 \cdot g^{-1}$, 0.01 $cm^3 \cdot g^{-1}$ and 9.4 nm, respectively. This can be attributed to the compacted structure of the assembly as have been demonstrated by SEM observations. In comparison with the x%-ZnO-500 series samples, x%-ZnO-700 series ones show a narrow hysteresis loop and the capillary condensation steps shift to a higher relative pressure (Fig. 6e–h), implying the reduction of porosity [30]. The values of the BET surface area, total pore volume and average pore diameter of the x%-ZnO-500 and x%-ZnO-700 series samples are summarized in Table 2.

From the table it can be seen that the specific surface area of the x%-ZnO-700 series samples is lower than those of the x%-ZnO-500 series ones, and this can be ascribed to the sintering effect to the ZnO nanocrystals at a high temperature, which reduces the pore diameter and also the total pore volume of their assemblies. For the four different x%-ZnO-500 samples, the specific surface area decreases with the increase of mass ratio of cellulose in their precursors. It is probably due to the compact arrangement of the ZnO

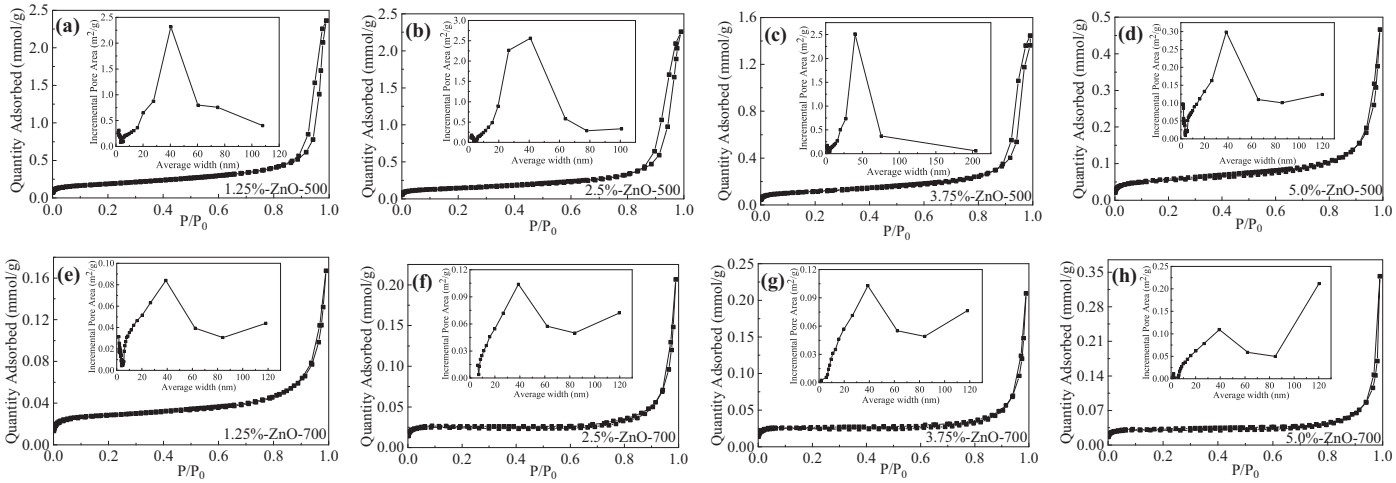

Fig. 6. The nitrogen adsorption–desorption isotherms and corresponding pore size distribution curves (inset) of x%-ZnO-500 series samples (a–d) and x%-ZnO-700 series samples (e–h).

Table 2
Specific surface area, pore volume and average pore width of x%-ZnO-500 and x%-ZnO-700 series samples.

Sample	Specific surface area ($m^2 \cdot g^{-1}$)	Pore volume ($cm^3 \cdot g^{-1}$)	Average pore width (nm)
1.25%-ZnO-500	14.8	0.06	15.9
2.5%-ZnO-500	11.7	0.06	22.3
3.75%-ZnO-500	9.3	0.05	20.4
5.0%-ZnO-500	4.5	0.01	9.4
1.25%-ZnO-700	2.1	0.004	8.0
2.5%-ZnO-700	2.2	0.004	7.4
3.75%-ZnO-700	2.2	0.004	7.7
5.0%-ZnO-700	2.6	0.005	7.7

nanocrystals at low cellulose content (as seen in Fig. 3A–D). While, for the x%-ZnO-700 series samples, they show quite similar specific surface area values even though they were derived from zincoxen cellulose solution with different contents of cellulose. This can be put down to the growth of ZnO nanocrystal size at a high calcinations temperature of 700 °C (see Fig. 3E–H). The specific surface area in somehow relates to the photocatalytic performance of the ZnO nanocrystal assemblies [31], which then influence the degradation rate of MO.

3.5. Photoluminescent properties

Fig. 7 depicts the photoluminescence curves of the two series of ZnO samples. From the figure, one can see that all the PL spectra consist of two emission bands located in UV and visible light regions, respectively. The strong UV emission at around 397 nm is attributed to the excitonic recombination of the near-band-edge (NBE) emission, while the peak in the visible ranges from 450 to 650 nm results from the defect states, such as Zn vacancies (V_{Zn}), O vacancies (V_O), interstitial Zn (Zn_i) and interstitial O (O_i). The PL spectra of x%-ZnO-500 series samples are shown in Fig. 7a. From the figure it can be seen that the UV emission peaks show an obvious blue-shift with the decrease of the content of cellulose in the precursors. This result can be ascribed to the broadening of the optical bandgaps [32]. For the x%-ZnO-700 series samples, no appreciable shift of the NBE emission band and a broad visible emission band can be observed (see in Fig. 7b). There are many reports on the emission properties of ZnO crystals and most of them show the green emissions at around 512 nm is more intense than the blue bands at about 455 and 459 nm. However, in our study it can be observed that the blue emission peaks is higher in comparison with the green ones for the x%-ZnO-500 series samples. The blue emission peak observed at about 455 and 459 nm, can be ascribed to the transition of electron from Zn_i to V_{Zn}, and the other blue emission which is around 480 and 483 nm may result from the electron transition between the V_O and O_i [33,34]. The green emission peak at around 510 and 512 nm corresponds to the singly ionized oxygen vacancy in ZnO and results from the recombination of a photogenerated hole with the singly ionized charge state of this defect. Therefore, the intensity of the green luminescence can be utilized to estimate the density of singly ionized oxygen vacancies [35–37]. As can be seen from Fig. 7a the intensity of green emission peak for the x%-ZnO-500 series samples follows the order of 2.5%-ZnO-500 > 3.75%-ZnO-500 > 5.0%-ZnO-500 > 1.25%-ZnO-500, while the peak intensity of green emission peak follows in an order of 5.0%-ZnO-700 > 3.75%-ZnO-700 > 2.5%-ZnO-700 > 1.25%-ZnO-700 for the x%-ZnO-700 series ones (see Fig. 7b), therefore, so does the content of oxygen vacancies in them.

3.6. Photocatalytic activity

Photocatalytic performances of x%-ZnO-500 and x%-ZnO-700 series samples are investigated on the basis of MO degradation under UV irradiation. The panels a and b in Fig. 8 shows the variation of the UV–visible absorption spectra of MO solution in the presence of ZnO nanocrystal assemblies under dark conditions for 3 h and under UV light irradiation for the same time in the absence of ZnO catalyst, respectively. As has been shown in Fig. 8, the MO exhibits a strong absorption at about 464 nm and a weak absorption at about 271 nm, which can be attribute to the absorptions of azo linkage and the phenyl chromophores in the organic molecules, respectively [9]. No degradation of MO is observed at the conditions of UV irradiation without ZnO or with ZnO catalyst but under dark conditions. From the control experiments, one can deduce that UV irradiation

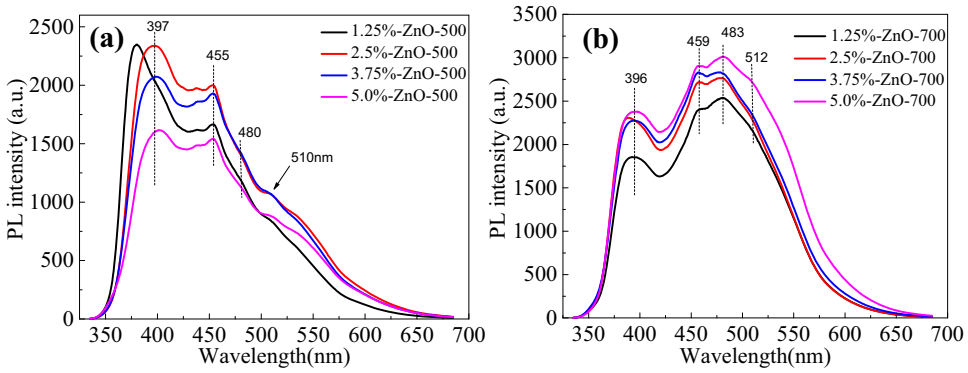

Fig. 7. Photoluminescence spectra of (a) x%-ZnO-500 series, and (b) x%-ZnO-700 series samples.

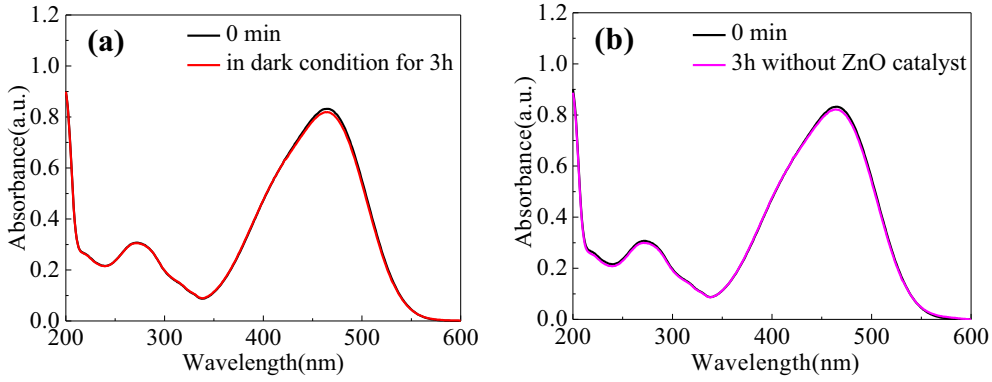

Fig. 8. UV–vis spectra of the MO solution stayed for 3 h, (a) with ZnO catalyst in a dark condition, and (b) under UV irradiation without ZnO catalyst.

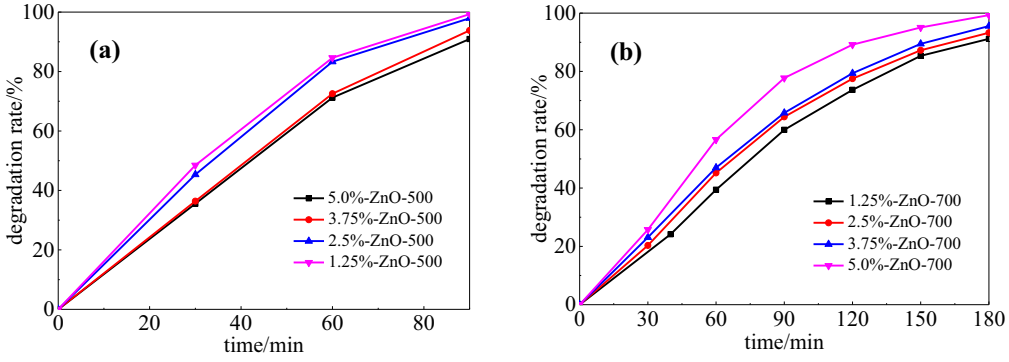

Fig. 9. Degradation ratio for (a) x%-ZnO-500 series samples, and (b) x%-ZnO-700 series ones.

and the presence of ZnO catalyst are two required essential factors for the photocatalytic degradation of MO. The degradation ratio D*r* can be calculated using the following formula:

$$Dr = (A_0 - A_t)/A_0 \times 100\%$$

Where A_0 is the initial absorbance at the characteristic absorption wavelength of 464 nm, A_t is the absorbance of the MO aqueous solution at time t.

Fig. 9 shows the plot of degradation ratio versus irradiation time. The MO degradation ratio with 1.25%-ZnO-500 catalyst reached to nearly 100% for 90 min, meanwhile, catalysts 2.5%-ZnO-500, 3.75%-ZnO-500 and 5.0%-ZnO-500 presented slightly low activities and showed of 97.94, 93.83 and 90.93% degradation ratios, respectively (see Fig. 9a). While, MO degradation ratio of about 100% took place in 180 min for 5.0%-ZnO-700 catalyst, nevertheless, the degradation ratios for 1.25%-ZnO-700, 2.5%-ZnO-700, 3.75%-ZnO-700 catalyst reached just to nearly 91.2, 93.3 and 95.6%, respectively, in the same time. From the results, it can be seen that both the two series of ZnO nanocrystal assemblies possess considerably high photoactivity under UV irradiation, and the x%-ZnO-500 series samples displayed higher photocatalytic activity than the x%-ZnO-700 series ones on the longitudinal comparison of them. Moreover, the 1.25%-ZnO-500 sample showed superior photocatalytic activity than the others. There can be many factors influencing the photocatalytic activity of ZnO nanocrystals such as specific surface area [38], crystal size [39], particle morphology [40], and oxygen vacancy [41]. In the following sections, these issues will be addressed and be discussed in order to illustrate the photocatalytic activities of different ZnO samples.

The mechanism for the photocatalytic degradation of dyes on the basis of ZnO nanocrystals is illustrated in Fig. 10 [42–44]. The band-edge positions of the ZnO crystal and the redox potential of

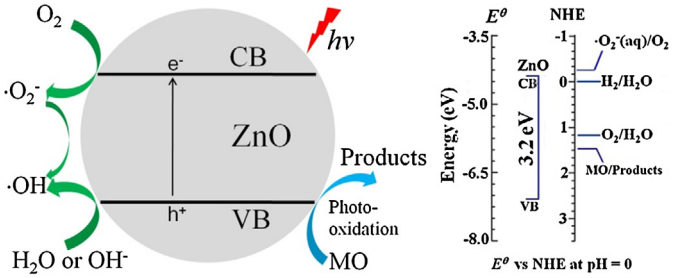

Fig. 10. Schematic illustration of the photocatalytic process with ZnO nanocrystals and the band-edge positions of the ZnO crystal and the redox potential of MO vs NHE.

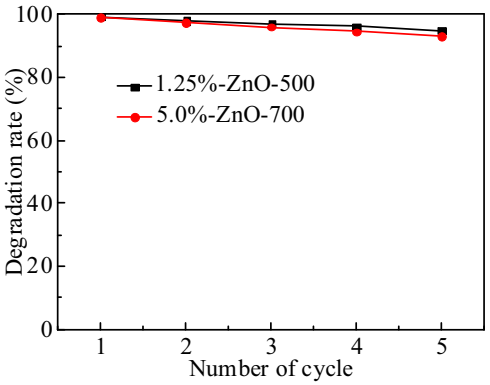

Fig. 11. Recycled degradation ratio of MO in the presence of ZnO nanocrystal assemblies under UV light irradiation.

MO measured by cyclic voltammetry vs NHE are also presented in the scheme [45].

When the ZnO nanocrystals are illuminated by UV light with energy larger than or equal to the energy of the band gap, the electrons are excited and transfer from the valence band (VB) to the conduction band (CB), leaving an equal number of vacant sites (holes). Subsequently, there can be two kinds of fate to the charge carriers [46]. The photo-excited electrons and the holes can recombine to liberate heat, and they can also migrate to the surface of the nanocrystals and act as reducing or oxidizing agents, respectively. The high oxidative potential of h^+_{VB} permits the direct oxidation of MO to reactive intermediates since the redox potential of MO is much higher than the VB band-edge of ZnO (Eq. (1)) [47].

$$h^+_{VB} + \text{dye} \rightarrow \text{dye}^{\bullet +} \rightarrow \text{photooxidation of MO dye} \quad (1)$$

Holes can also react with hydroxide anions or water molecules to form highly reactive hydroxyl radicals (•OH) which is a strong and nonselective oxidant owning ability to degrade dyes. (Eqs. (2) and (3)).

$$h^+_{VB} + OH^- \rightarrow {}^{\bullet}OH \quad (2)$$

$$h^+_{VB} + H_2O \rightarrow {}^{\bullet}OH + H^+ \quad (3)$$

Meanwhile, conduction band electron e^-_{CB} can be captured by preadsorbed oxygen molecules (O_2) on catalyst surface to form reactive oxygen species ($^{\bullet}O_2^-$), which reacts with H^+ and results further in the formation of oxidative •OH radicals, (Eqs. (4)–(7)):

$$O_2 + e^-_{CB} \rightarrow {}^{\bullet}O_2^- \quad (4)$$

$$^{\bullet}O_2^- + H^+ \rightarrow HOO^{\bullet} \quad (5)$$

$$HOO^{\bullet} + H^+ + e^-_{CB} \rightarrow H_2O_2 \quad (6)$$

$$H_2O_2 + h\nu \rightarrow {}^{\bullet}OH + OH^- \quad (7)$$

Alternatively, the reactive oxygen species ($^{\bullet}O_2^-$) can also reacted directly with MO molecules, resulting in degrading of MO through a photoreduction process (Eq. (8)) [48].

$$^{\bullet}O_2^- + \text{MO} \rightarrow \text{Products} \quad (8)$$

Based on the above-mentioned results and the proposed mechanism, we can then elucidate the influence factors on the catalytic activities of these ZnO nanocrystals. First, the large surface area in the assembly of ZnO naocrystal can offer more active sites and allow more opportunity for the mass transportation of reactant/product molecules. (see Table 2). Second, the grain sizes of x%-ZnO-500 series samples are smaller than that of the x%-ZnO-700 series ones. On the one hand, the smaller of the nanocrystals, the higher of the specific surface area. On the other hand, with the decrease of the crystal size the distance of photo-generated electrons and holes moving from internal to the surface is shorten, thus promote the process of photo degradation. Third, it is well-known that the crystal morphologies play also important role on the photocatalytic performance of ZnO nanocrystals since the photocatalytic activity is strongly depends on some specific exposed crystal faces [49,50]. However, such a specific crystal faces is still open questions to answer. It should be stated that essential understanding of these questions demands much deeper experimental and theoretical work. Fourth, as can be seen from the photoluminescence study, there are abundant oxygen vacancies in the ZnO nanocrystals and its content can be estimated by analyzing the intensity of the green emission peak. The oxygen vacancies have been proved to be favorable for the efficient separation of electron–hole pairs and minimize the radiative recombination of electron and hole [51]. What's more, oxygen vacancy can promote oxygen adsorption and then generate active component of superoxide radical anion ($^{\bullet}O_2^-$), which is beneficial to the photocatalytic ability of ZnO particles [52,53]. As for the superiority in photocatalytic efficiency of the x%-ZnO-500 series samples than that of the x%-ZnO-700 series ones, and the prominent photocatalytic activity of the 1.25%-ZnO-500 sample, all these factors mentioned above should be taken into account.

3.7. Recyclability and stability

Excellent reusability and high stability are of great significance to evaluate the quality of a catalyst. The 1.25%-ZnO-500 and 5.0%-ZnO-700 samples were selected to study the reusability, and both the two ZnO samples were tested for five successive cycles. Fig. 11 shows the cycled photocatalytic degradation of MO in the presence of ZnO nanocrystal assemblies under UV light irradiation. The degradation ratios higher than 93% are observed for both the samples even after five catalytic cycles. Such a high recyclability can be attributed to the assembly structure of the catalysts, which prevent the catalyst from leaching during the recycle process. Satisfyingly, both the samples show quite similar XRD patterns (which corresponds to the hexagonal wurtzite structure of ZnO) and morphology with the as-prepared ones, indicating their high composition and structure stability (see Figs. S3 and S4).

4. Conclusions

The large-scale producible spray drying processes has been demonstrated to be a simple and unique approach to the preparation of ZnO nanocrystal assemblies by simply combining it with a calcinations step. The conventional zincoxen cellulose aqueous solution has been used as raw materials for the preparation and it provides both the precursor for ZnO and the sacrificial template for assembling of the nanocrystals. The size of individual ZnO nanocrystal, morphology of the assembly and the photoluminescent property are relative to the content of the sacrificial

template of cellulose and also to the applied calcinations temperatures. The resultant ZnO nanocrystal assemblies show high photocatalytic activity in the degradation of methyl orange dyes. It has been demonstrated that an assembly with large specific surface area and consist of small-sized nanocrystals with suitable density of surface oxygen vacancy is desirable for the photocatalytic reactivity. All in all, both the developed preparation method and the resulted ZnO nanocrystal assemblies show great potentials in practical application.

Acknowledgments

This work is supported by the National Key Project on Basic Research (Grant No 2012CB722705) and the National High Technology Research and Development Program (NO. 2014AA250323) of China. This work is also financially supported by the National Natural Science Foundation of China (No.51407134) and China Postdoctoral Science Foundation (No.2016M590619). We acknowledge the Taishan Scholars Advantageous and Distinctive Discipline Program of Shandong Province for supporting the research team of energy storage materials. Y. Wang would like to thank the financial support from the Top-notch Innovative Talent Program of Qingdao City (Grant no.: 13-CX-8).

Appendix A. Supplementary data

Supplementary data associated with this article can be found, in the online version, at http://dx.doi.org/10.1016/j.colsurfa.2017.02.068.

References

[1] X. Zhong, W. Knoll, Morphology-controlled large-scale synthesis of ZnO nanocrystals from bulk ZnO, Chem. Commun. 36 (2005) 1158–1160.
[2] X. Kong, X. Sun, X. Li, Y. Li, Catalytic growth of ZnO nanotubes, Mater. Chem. Phys. 82 (2003) 997–1001.
[3] J. Song, S. Lim, Effect of seed layer on the growth of ZnO nanorods, J. Phys. Chem. C 111 (2006) 596–600.
[4] T. Sun, J. Qiu, C. Liang, Controllable fabrication and photocatalytic activity of ZnO nanobelt arrays, J. Phys. Chem. C 112 (2008) 715–721.
[5] X. Wang, Y. Ding, Z. Li, J. Song, Z.L. Wang, Single-crystal mesoporous ZnO thin films composed of nanowalls, J. Phys. Chem. C 113 (2009) 1791–1794.
[6] Y. Ding, F. Zhang, Z.L. Wang, Deriving the three-dimensional structure of ZnO nanowires/nanobelts by scanning transmission electron microscope tomography, Nano Res. 6 (2013) 253–262.
[7] P.K. Samanta, A. Saha, Wet chemical synthesis of ZnO nanoflakes and photoluminescence, Optik 126 (2015) 3786–3788.
[8] H. Yu, H. Fan, X. Wang, J. Wang, P. Cheng, Synthesis of flower-like ZnO nanostructures by sonochemical route and their photocatalytic activity, Optik 126 (2015) 4397–4400.
[9] Q.L. Ma, R. Xiong, B.G. Zhai, Y.M. Huang, Ultrasonic synthesis of fern-like ZnO nanoleaves and their enhanced photocatalytic activity, Appl. Surf. Sci. 324 (2015) 842–848.
[10] A. Rayerfrancis, P.B. Bhargav, N. Ahmed, B. Chandra, S. Dhara, Effect of pH on the morphology of ZnO nanostructures and its influence on structural and optical properties, Physica B 457 (2015) 96–102.
[11] C.L. Wu, L. Chang, H.G. Chen, C.W. Lin, T.F. Chang, Growth and characterization of chemical-vapor-deposited zinc oxide nanorods, Thin Solid Films 498 (2006) 137–141.
[12] H. Chik, J. Liang, S.G. Cloutier, N. Kouklin, J.M. Xu, Periodic array of uniform ZnO nanorods by second-order self-assembly, Appl. Phys. Lett. 84 (2004) 3376–3378.
[13] M. Vafaee, M.S. Ghamsari, Preparation and characterization of ZnO nanoparticles by a novel sol–gel route, Mater. Lett. 61 (2007) 3265–3268.
[14] Y. Zeng, T. Zhang, L. Qiao, Preparation and gas sensing properties of the nutlike ZnO microcrystals via a simple hydrothermal route, Mater. Lett. 63 (2009) 843–846.
[15] D. Klemm, B. Heublein, H.P. Fink, A. Bohn, Cellulose: fascinating biopolymer and sustainable raw material, Angew. Chem. Int. Edit 44 (2005) 3358–3393.
[16] X. Cheng, A. Fu, H. Li, Y. Wang, P. Guo, J. Liu, J. Zhang, X.S. Zhao, Sustainable preparation of copper particles decorated carbon microspheres and studies on their bactericidal activity and catalytic properties, ACS Sustain. Chem. Eng. 3 (2015) 133.
[17] X. Qin, A. Lu, J. Cai, L. Zhang, Stability of inclusion complex formed by cellulose in NaOH/urea aqueous solution at low temperature, Carbohyd. Polym. 92 (2013) 1315–1320.
[18] Q. Wang, A. Fu, H. Li, J. Liu, P. Guo, X.S. Zhao, L.H. Xia, Preparation of cellulose based microspheres by combining spray coagulating with spray drying, Carbohyd. Polym. 111 (2014) 393–399.
[19] M. Wang, Y. Zhang, Y. Zhou, F. Yang, E.J. Kim, Rapid room-temperature synthesis of nanosheet-assembled ZnO mesocrystals with excellent photocatalytic activity, CrystEngComm 15 (2012) 754–763.
[20] J. Cui, J. Sun, X. Liu, J. Li, X. Ma, Fabrication of hierarchical flower-like porous ZnO nanostructures from layered $ZnC_2O_4 \cdot 3Zn(OH)_2$ and gas sensing properties, Appl. Surf. Sci. 308 (2014) 17–23.
[21] Q. Chang, Z. Ma, J. Wang, Y. Yan, W. Shi, Graphene nanosheets@ZnO nanorods as three-dimensional high efficient counter electrodes for dye sensitized solar cells, Electrochim. Acta 151 (2015) 459–466.
[22] L. Xu, Z. Li, Q. Cai, H. Wang, H. Gao, Precursor template synthesis of three-dimensional mesoporous ZnO hierarchical structures and their photocatalytic properties, CrystEngComm 12 (2010) 2166–2172.
[23] L. Zhang, G. Yang, W. Fang, Regenerated cellulose membrane from cuoxam/zincoxene blend, J. Membrane Sci. 56 (1991) 207–215.
[24] D.A.A. Santos, A.D.P. Rocha, M.A. Macêdo, Rietveld refinement of transition metal doped ZnO, Powder Diffr. Suppl. 23 (2) (2008) S36–S41.
[25] Q. Chang, H. Zhang, X. Wang, W. Shao, H. Li, F. Yuan, X. Xu, S. Xu, Structure and electrochemical performance of hollow microspheres of $LiFe_xNi_{1/3-x}Co_{1/3}Mn_{1/3}O_2$ ($0.0000 \leq X \geq 0.267$) as cathodes for lithium-ion batteries, RSC Adv. 5 (2015) 56274–56278.
[26] L.C. Nehru, V. Swaminathan, C. Sanjeeviraja, Rapid synthesis of nanocrystalline ZnO by a microwave-assisted combustion method, Powder Tech. 226 (2012) 29–33.
[27] F. Vaz, L. Rebouta, Ph. Goudeau, J.P. Riviere, E. Schaffer, G. Kleer, M. Bodmann, Residual stress states in sputtered $Ti_{1-x}Si_xN_y$ films, Thin Solid Films 402 (2002) 195–202.
[28] J. Michlera, M. Mermoux, Y. von Kaenel, A. Haouni, G. Lucazeau, E. Blank, Residual stress in diamond films: origins and modeling, Thin Solid Films 357 (1999) 189–201.
[29] H. Li, J. Sang, J. Zhao, A. Fu, H. Liu, M. Xu, G. Pang, X.S. Zhao, Preparation of magnetically separable mesoporous Co@carbon/silica composites by the RAPET method, New J. Chem. 36 (2012) 2308–2315.
[30] D. Wang, A. Fu, H. Li, Y. Wang, J. Liu, P. Guo, X.S. Zhao, Mesoporous carbon spheres with controlled porosity for high-performance lithium-sulfur batteries, J. Power Sources 285 (2015) 469–477.
[31] Z. Liu, Z. Liu, T. Cui, J. Li, J. Zhang, Photocatalysis of two-dimensional honeycomb-like ZnO nanowalls on zeolite, Chem. Eng. J. 235 (2014) 257–263.
[32] L. Xu, J. Su, Y. Chen, G. Zheng, S. Pei, Optical and structural properties of ZnO/ZnMgO composite thin films prepared by sol–gel technique, J. Alloy. Compd. 548 (2013) 7–12.
[33] N.S. Sabri, A.K. Yahya, M.K. Talari, Emission properties of Mn doped ZnO nanoparticles prepared by mechanochemical processing, J. Lumin. 132 (2012) 1735–1739.
[34] A. Mahroug, S. Boudjadar, S. Hamrit, L. Guerbous, Structural, morphological and optical properties of undoped and Co-doped ZnO thin films prepared by sol–gel process, J. Mater. Sci.-Mater. El. 25 (2014) 4967–4974.
[35] A.B. Patil, K.R. Patil, S.K. Pardeshi, Ecofriendly synthesis and solar photocatalytic activity of S-doped ZnO, J. Hazard. Mater. 183 (2010) 315–323.
[36] R. Yousefi, B. Kamaluddin, The effects of annealing temperature on structural and optical properties of S-doped ZnO nanobelts, Solid State Sci. 12 (2010) 252–256.
[37] C. Hariharan, Photocatalytic degradation of organic contaminants in water by ZnO nanoparticles: revisited, Appl. Catal. A: Gen. 304 (2006) 55–61.
[38] G. Poongodi, P. Anandan, R.M. Kumar, R. Jayavel, Studies on visible light photocatalytic and antibacterial activities of nanostructured cobalt doped ZnO thin films prepared by sol–gel spin coating method, Spectrochim. Acta A 148 (2015) 237–243.
[39] D. Jiang, C. Xing, X. Liang, L. Shao, M. Chen, Synthesis of cuprous oxide with morphological evolution from truncated octahedral to spherical structures and their size and shape-dependent photocatalytic activities, J. Colloid Interf. Sci. 461 (2016) 25–31.
[40] D. Li, H. Haneda, Morphologies of zinc oxide particles and their effects on photocatalysis, Chemosphere 51 (2003) 129–137.
[41] L. Jing, Z. Xu, X. Sun, J. Shang, W. Cai, The surface properties and photocatalytic activities of ZnO ultrafine particles, Appl. Surf. Sci. 180 (2001) 308–314.
[42] H. Tong, S. Ouyang, Y. Bi, N. Umezawa, M. Oshikiri, Nano-photocatalytic Materials: Possibilities and Challenges, Adv. Mater 24 (2012) 229–251.
[43] C. Yan, Z. Hua, B. Liu, H. Yang, Charge separation between wurtzite ZnO polar {001 surfaces and their enhanced photocatalytic activity, Appl. Catal. B: Environ. 163 (2015) 189–197.
[44] B. Li, Y. Wang, Facile Synthesis, Enhanced photocatalytic performance of flower-like ZnO hierarchical microstructures, J. Phys. Chem. C 114 (2009) 890–896.
[45] H. Tong, S. Ouyang, Y. Bi, N. Umezawa, M. Oshikiri, J. Ye, Nano-photocatalytic materials: possibilities and challenges, Adv. Mater. 24 (2012) 229–251.
[46] R. Kumar, G. Kumar, A. Umar, Zinc oxide nanomaterials for photocatalytic degradation of methyl orange: a review, Nanosci. Nanotech. Lett. 6 (8) (2014) 631–650.
[47] F. Xu, Y. Shen, L. Sun, H. Zeng, Y. Lu, Enhanced photocatalytic activity of hierarchical ZnO nanoplate-nanowire architecture as environmentally safe and facilely recyclable photocatalyst, Nanoscale 3 (2011) 5020–5025.

[48] S.C. Yan, Z.S. Li, Z.G. Zou, Photodegradation of Rhodamine B and Methyl Orange over Boron-Doped g-C_3N_4 under visible light irradiation, Langmuir 26 (6) (2010) 3894–3901.
[49] Y. Yamaguchi, M. Yamazaki, S. Yoshihara, T. Shirakashi, Photocatalytic ZnO films prepared by anodizing, J. Electroanal. Chem 442 (1998) 1–3.
[50] J. Xie, Y. Li, W. Zhao, L. Bian, Y. Wei, Simple fabrication and photocatalytic activity of ZnO particles with different morphologies, Powder Technol. 207 (2011) 140–144.
[51] J. Yang, X. Kong, W. Jiang, J. Cao, P. Zou, Size-controllable synthesis and photocatalytic performance of ZnO hollow spheres, Mat. Sci. Semicon. Pro. 40 (2015) 713–719.
[52] N.H. Linh, T.Q. Nguyen, W.A. Diño, H. Kasai, Effect of oxygen vacancy on the adsorption of O2on anatase TiO2(001): A DFT-based study, Surf. Sci. 633 (2015) 38–45.
[53] J. Kaur, S. Singhal, Facile synthesis of ZnO and transition metal doped ZnO nanoparticles for the photocatalytic degradation of methyl orange, Ceram. Int. 40 (2014) 7417–7424.